

Understanding the role of surface states in the electrical response of semiconductor–electrolyte interfaces from first principles

Quinn Campbell* and Ismaila Dabo

*Department of Materials Science and Engineering, Materials Research Institute,
and Penn State Institutes of Energy and the Environment,
The Pennsylvania State University, University Park, PA 16802, USA*

A broad range of electrochemical reactions of foremost technological interest occur at the interface between a semiconductor and an electrolyte. We present a first-principles method to study these interfaces, whereby a quantum treatment of the surface states that are induced by the adsorption of ionic species is embedded into a continuum description of the bending of the electronic bands within the depletion region of the semiconductor electrode. The full analytical formulation of the interface energy is presented and its minimization under typical doping and electrolytic conditions is derived. The model is validated by studying Si(110), SiO₂(110), and rutile TiO₂(110) electrodes; it correctly captures the instability of silicon in water and demonstrates the dominance of surface states in the behavior of the interfacial electrostatic potential. The new computational method provides microscopic insights into the low-voltage regime where surface states determine the overall electrical response of the electrified semiconductor–solution interface.

I. INTRODUCTION

Predicting the electrical response of semiconductor–electrolyte interfaces is of ultimate relevance to a vast array of electrochemical and photochemical systems; these interfaces are involved in the photocatalytic splitting of water,¹ the photoreduction of carbon dioxide into hydrocarbons,² the electrochemical etching of semiconductor surfaces,^{3–5} the storage of energy at metal oxide electrodes,⁶ and the use of quantum dots as biological markers.⁷ The central role played by semiconductor electrodes at the frontier between condensed matter physics and electrochemistry provides a compelling motivation to study their stability in realistic ionic environments.

Density-functional theory calculations have been extensively used to accelerate the search for new photocatalysts,^{8–10} assess the alignment of the valence and conduction bands of semiconductor electrodes with the redox potentials of species in solution,^{11–15} determine reaction pathways,^{16–18} and elucidate the dynamical interactions of the solvent molecules with the surface of the semiconductor.^{19–22} The same calculations can, in principle, be applied to predict the electrical response of semiconductor–solution interfaces as long as they correctly account for the long-range decay of the electrostatic potential within the semiconductor depletion region. However, electrostatic screening is much less effective in doped semiconductors than it is in metals,²³ causing the interfacial electric field to penetrate up to 10–10³ nm into the electrode for typical dopant concentrations of 10¹⁶–10¹⁸ cm⁻³. These length scales render the explicit first-principles simulation of the interface prohibitively expensive with available multicore computer resources.

Therefore, it is necessary to develop simplified first-principles models that will capture the essential features of a semiconductor–electrolyte interface at reduced computational cost. To this end, we exploit and further develop the newly released self-consistent solvation model

proposed by Andreussi et al.²⁴ to simulate semiconductor electrodes under applied voltage in electrolytic media. While this method has been successful in modeling solvated metal electrodes,^{25–29} no previous study has accounted for the effects of band bending and surface states at semiconductor electrodes.

In order to provide a clear illustration of band bending, the electronic levels at the surface of a semiconductor electrode are shown in Fig. 1. Here, it is seen that the bending of the bands is caused by the initial difference in the Fermi level of the semiconductor and the equilibrium potential of the dominant redox couple in the solution. To reach equilibrium, these levels must be aligned and charge must be transferred between the semiconductor and the solution. Since the excess charge is accommodated within semiconductors by a relatively low concentration of dopants, the electrostatic potential is seen to decay gradually across the extended depletion region.

In this work, we present a quantum–continuum interface model to describe this long-range decay and simulate the response of semiconductor–electrolyte interfaces under electrification, including the influence of the surface states resulting from the adsorption of ionic species at the semiconductor surface. We demonstrate the performance of the model for solvated Si(110) and SiO₂(110) electrodes, and then exploit its unique predictive performance to answer critical questions regarding the role of surface states in the response of oxygenated and hydrogenated TiO₂(110) electrodes in aqueous electrolytes.

II. METHOD

A. Interface energy

The first step in constructing the model is to partition the system into the three regions shown in Fig. 2. Region (I) represents the bulk of the semiconductor, which will

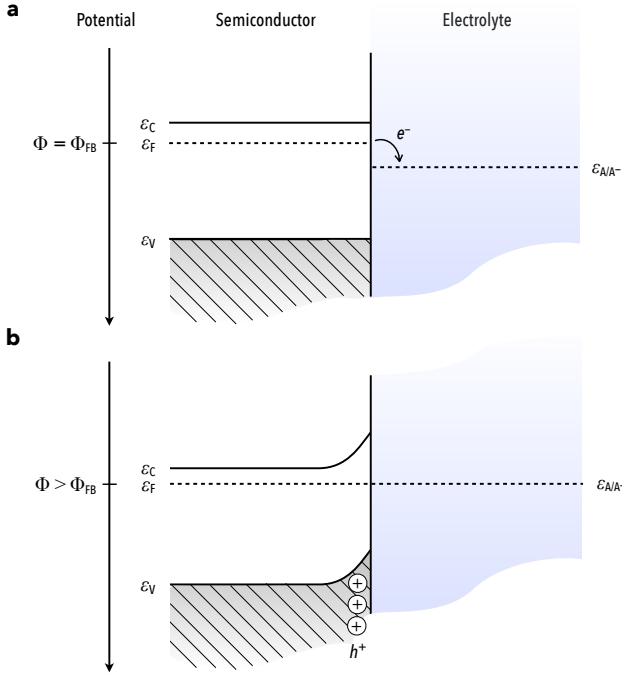


FIG. 1. A semiconductor–electrolyte interface (a) in its initial non-equilibrium state and (b) after equilibrium. To align the Fermi energy of the semiconductor with the redox potential of the electrolyte, charge must be transferred between the semiconductor and redox couples in solution, resulting in the buildup of interfacial charge and band bending. The flat-band potential, Φ_{FB} , corresponds to the opposite of the Fermi level of the neutral semiconductor electrode. The new Fermi level at equilibrium then represents the potential, Φ , of the semiconductor electrode.

be modeled at the continuum level. Region (II) corresponds to the surface of the electrode; this region will be described quantum mechanically to accurately represent the adsorbed species and resulting surface states. Region (III) denotes the electrolytic solution, which consists of a diffuse distribution of ions in a polarizable continuum. Also illustrated in Fig. 2 is the flatband potential Φ_{FB} , which corresponds to the difference between the asymptotic value φ_∞ of the potential inside Region (I) and the Fermi energy of the neutral slab:

$$\Phi_{\text{FB}} = \varphi_\infty - \epsilon_{\text{F}}. \quad (1)$$

Having defined these three regions, the free energy of the system is written as

$$F = F_{\text{(I)}} + F_{\text{(II)}} + F_{\text{(III)}} - \frac{1}{2} \int d\mathbf{r} \epsilon_0 \epsilon(\mathbf{r}) |\nabla \varphi(\mathbf{r})|^2, \quad (2)$$

where ϵ denotes the space-dependent dielectric permittivity across the interface, and $F_{\text{(I)}}$, $F_{\text{(II)}}$, and $F_{\text{(III)}}$ stand for the free energies of the continuum space charge, quantum surface slab, and continuum electrolyte, respectively.

This dielectric permittivity is defined using the self-consistent continuum solvation model.²⁴ In this model a

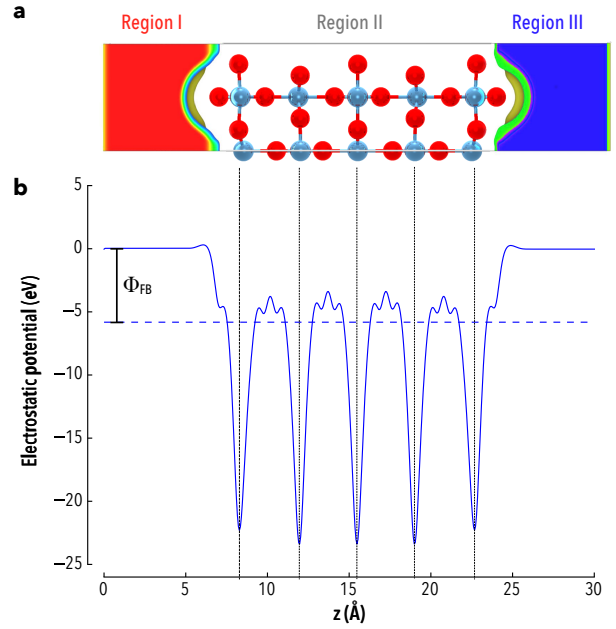


FIG. 2. (a) Partition of a TiO_2 –electrolyte interface into three regions. Region (I) represents the continuum bulk semiconductor section, Region (II) the quantum surface of the semiconductor, and Region (III) the continuum electrolyte solution. Both Regions (I) and (III) extend infinitely. The colors indicate the changing dielectric constant in the simulation; red corresponds a dielectric constant of 170 for TiO_2 and blue corresponds to a dielectric constant of 78 for water at room temperature. (b) Profile of the electrostatic potential across the TiO_2 –electrolyte interface with the dotted horizontal line representing the Fermi level of the slab (ϵ_{F}). Having set the potential to cancel out at the boundaries of the cell, the flat-band potential (Φ_{FB}) equals the negative of the Fermi level.

dielectric cavity is created at each lateral facet. On the semiconductor side, the local dielectric permittivity can be written as $\epsilon(\mathbf{r}) = \exp[(\zeta(\mathbf{r}) - \sin(2\pi\zeta(\mathbf{r}))/2\pi) \ln \epsilon_{\text{(I)}}]$ where $\epsilon_{\text{(I)}}$ is the dielectric constant of the bulk of the semiconductor and $\zeta(\mathbf{r}) = (\ln \rho_{\text{max}} - \ln \rho(\mathbf{r})) / (\ln \rho_{\text{max}} - \ln \rho_{\text{min}})$ is used as a smooth switching function, marking the transition between the quantum and continuum regions. Here, ρ_{min} and ρ_{max} serve as the density thresholds specifying the inner and outer isocontours of the dielectric cavity. We employ the same parametrization in Region (III), replacing $\epsilon_{\text{(I)}}$ with $\epsilon_{\text{(III)}}$, the dielectric constant of the electrolyte. We specifically use $\rho_{\text{max}} = 5 \times 10^{-3}$ a.u. and $\rho_{\text{min}} = 10^{-4}$ a.u. for our calculations.

Focusing first on Region (I), the contribution to the free energy can be expressed in terms of the local density of negative charge carriers n and positive charge carriers

p as the sum of electrostatic and entropic terms:

$$\begin{aligned} F_{(I)} = & \int d\mathbf{r}(\varphi(\mathbf{r}) + \epsilon_V - \epsilon_F)p(\mathbf{r}) - Ts(p(\mathbf{r}), p_d(\mathbf{r})) \\ & - \int d\mathbf{r}(\varphi(\mathbf{r}) + \epsilon_C - \epsilon_F)n(\mathbf{r}) + Ts(n(\mathbf{r}), n_d(\mathbf{r})) \\ & - \int d\mathbf{r}\varphi(\mathbf{r})(n_d(\mathbf{r}) - p_d(\mathbf{r})) \end{aligned} \quad (3)$$

with

$$s(f, f_d) = -k_B \left[(f_d - f) \ln \left(1 - \frac{f}{f_d} \right) + f \ln \left(\frac{f}{f_d} \right) \right].$$

In Eq. (3), ϵ_F denotes the Fermi energy, ϵ_V is the electronic energy at the top of the valence band, and ϵ_C is the energy at the bottom of the conduction band. Furthermore, it is assumed that the donor and acceptor levels are shallow so that their energy levels sit at the band edges. Moreover, s stands for the Fermi–Dirac entropy; it depends locally on the smooth switching functions

$$\begin{aligned} n_d(\mathbf{r}) &= \frac{N_d}{2} \left[\operatorname{erfc} \left(\frac{z - z_{(I)}}{\sigma_{(I)}} \right) + 1 \right] \\ p_d(\mathbf{r}) &= \frac{P_d}{2} \left[\operatorname{erfc} \left(\frac{z - z_{(I)}}{\sigma_{(I)}} \right) + 1 \right] \end{aligned} \quad (4)$$

with N_d and P_d being the concentrations of electron-donating and electron-accepting defects, and $z_{(I)}$ and $\sigma_{(I)}$ being the location and spatial extent of the transition between the semiconductor and surface.

Likewise, the free energy of the electrolyte can be expressed in terms of the concentrations c_+ and c_- of the positive and negative ions as

$$\begin{aligned} F_{(III)} = & \int d\mathbf{r}\varphi(\mathbf{r})c_+(\mathbf{r}) - T\sigma(c_+(\mathbf{r}), c^\circ(\mathbf{r})) \\ & - \int d\mathbf{r}\varphi(\mathbf{r})c_-(\mathbf{r}) + T\sigma(c_-(\mathbf{r}), c^\circ(\mathbf{r})) \end{aligned} \quad (5)$$

with

$$\sigma(f, f^\circ) = -k_B \left[f \ln \left(\frac{f}{f^\circ} \right) - f \right]$$

In Eq. (5), we take a symmetric 1:1 ionic solution, in which the maximal ion concentration is defined as

$$c^\circ(\mathbf{r}) = \frac{c_{\text{eq}}^\circ}{2} \left[\operatorname{erfc} \left(\frac{z_{(III)} - z}{\sigma_{(III)}} \right) + 1 \right], \quad (6)$$

where c_{eq}° is the equilibrium ionic concentration inside the electrolyte, and $z_{(III)}$ and $\sigma_{(III)}$ are the location and spread of the frontier between the surface and electrolyte.

Finally, the free energy $F_{(II)}$ is expressed as a Kohn–Sham functional of the density of the electrons ρ_- and distribution of the atomic cores ρ_+ :

$$\begin{aligned} F_{(II)} = & T_s + E_{\text{Hxc}} - \theta \mathcal{S} \\ & + \int d\mathbf{r}(\varphi(\mathbf{r}) - \epsilon_F)\rho_-(\mathbf{r}) - \varphi(\mathbf{r})\rho_+(\mathbf{r}) \end{aligned} \quad (7)$$

where T_s is the kinetic energy of the auxiliary system within the independent-electron mapping and E_{Hxc} is the sum of the Hartree and exchange–correlation energies. The electronic temperature and the entropy of the electronic smearing are denoted θ and \mathcal{S} , respectively.

B. Energy minimization

With the expression of the free energy F in hand, the equilibrium charge density can be obtained by variations of F with respect to the occupations of the doping levels, ionic concentrations, and electrostatic potential, yielding the following equations:

$$n(\mathbf{r}) = n_d(\mathbf{r}) \left\{ 1 + \exp \left(\frac{\varphi(\mathbf{r}) + \epsilon_C - \epsilon_F}{k_B T} \right) \right\}^{-1} \quad (8)$$

$$p(\mathbf{r}) = p_d(\mathbf{r}) \left\{ 1 + \exp \left(\frac{\epsilon_F - \epsilon_V - \varphi(\mathbf{r})}{k_B T} \right) \right\}^{-1} \quad (9)$$

$$c_\pm(\mathbf{r}) = c^\circ(\mathbf{r}) \exp \left(\mp \frac{\varphi(\mathbf{r})}{k_B T} \right) \quad (10)$$

$$\begin{aligned} \nabla(\epsilon_0 \epsilon(\mathbf{r}) \nabla \varphi(\mathbf{r})) = & p(\mathbf{r}) - n(\mathbf{r}) + p_d(\mathbf{r}) - n_d(\mathbf{r}) \\ & + c_+(\mathbf{r}) - c_-(\mathbf{r}) + \rho_+(\mathbf{r}) - \rho_-(\mathbf{r}), \end{aligned} \quad (11)$$

where it is understood that ρ_- is obtained by solving the self-consistent Kohn–Sham equation for a given distribution ρ_+ of the atomic cores.

It should be mentioned that for a n -type semiconductor, using the Boltzmann statistics approximation, these equations become

$$p(\mathbf{r}) = p_d(\mathbf{r}) = 0 \quad (12)$$

$$n(\mathbf{r}) = n_d(\mathbf{r}) \exp \left(\frac{\varphi_\infty - \varphi(\mathbf{r})}{k_B T} \right), \quad (13)$$

where φ_∞ stands for the asymptotic value of the potential in Region (I). Conversely, for a p -type semiconductor, we can write

$$n(\mathbf{r}) = n_d(\mathbf{r}) = 0 \quad (14)$$

$$p(\mathbf{r}) = p_d(\mathbf{r}) \exp \left(\frac{\varphi(\mathbf{r}) - \varphi_\infty}{k_B T} \right). \quad (15)$$

Before explaining the computational solution of these equations, it is important to note that deep inside the semiconductor region, the electrostatic potential obeys the one-dimensional Poisson equations:

$$\frac{d^2 \varphi}{dz^2} = \frac{N_d}{\epsilon_0 \epsilon_{(I)}} \left[1 - \exp \left(\frac{\varphi_\infty - \varphi}{k_B T} \right) \right] \quad (16)$$

$$\frac{d^2\varphi}{dz^2} = \frac{P_d}{\epsilon_0\epsilon_{(I)}} \left[\exp\left(\frac{\varphi - \varphi_\infty}{k_B T}\right) - 1 \right] \quad (17)$$

under conditions of *n*-type and *p*-type doping, respectively. In the long-range limit where φ approaches φ_∞ , these equations imply

$$\left(\frac{d\varphi}{dz}\right)^2 = \frac{2N_d}{\epsilon_0\epsilon_{(I)}} \left[\varphi - \varphi_\infty + k_B T \left(e^{\frac{\varphi - \varphi_\infty}{k_B T}} - 1 \right) \right] \quad (18)$$

$$\left(\frac{d\varphi}{dz}\right)^2 = \frac{2P_d}{\epsilon_0\epsilon_{(I)}} \left[\varphi_\infty - \varphi + k_B T \left(e^{\frac{\varphi - \varphi_\infty}{k_B T}} - 1 \right) \right]. \quad (19)$$

These asymptotic expressions can then be used to derive the standard Mott–Schottky capacitance. They will be critical to describing the bending of the electronic bands and overcome the length scales that characterize electrostatic screening in the depletion region of the electrode, as explained below.

C. Minimization method

To obtain the equilibrium free energy of the system, we place a plane of countercharge $q_{(I)}$ in Region (I), representing the defect charge in the bulk of the semiconductor, and another plane of countercharge $q_{(III)}$ in Region (III), representing the ionic charge of the electrolyte. Accordingly, an explicit charge $q_{(II)} = -q_{(I)} - q_{(III)}$ is added to the slab of Region (II) so that charge neutrality is fulfilled.

This planar setup provides an accurate approximation of the electrolytic side [Region (III)] of a semiconductor–electrolyte interface in the case of a concentrated electrolyte where the ionic concentrations (0.1–1 M) are significantly larger than typical doping concentrations in the semiconductor. This means that most of the potential drop takes place in the bulk of the semiconductor [Region (III)], making a plane of countercharge a reliable representation of the response of the electrolyte [Region (I)] (the Helmholtz model).

Furthermore, on the semiconductor side, it is important to mention that adding a plane of countercharge does not lead to any loss of generality in the solution of the problem. This can be seen by noting that once the Helmholtz plane of countercharges in Region (III) is set and the asymptotic boundary conditions of Poisson’s equation inside the electrolyte is fixed, the Fermi energy ϵ_F and charge density ρ_- at the surface are fully determined; they do not depend on the specific shape of the defect charge profile in virtue of Gauss’ law. In other words, the charge distribution and potential profile on the right hand side provide an accurate description of the interaction of the electrode with solution.

Although the electrostatic profile in Regions (II) and (III) is accurate, the potential in Region (I) is still not

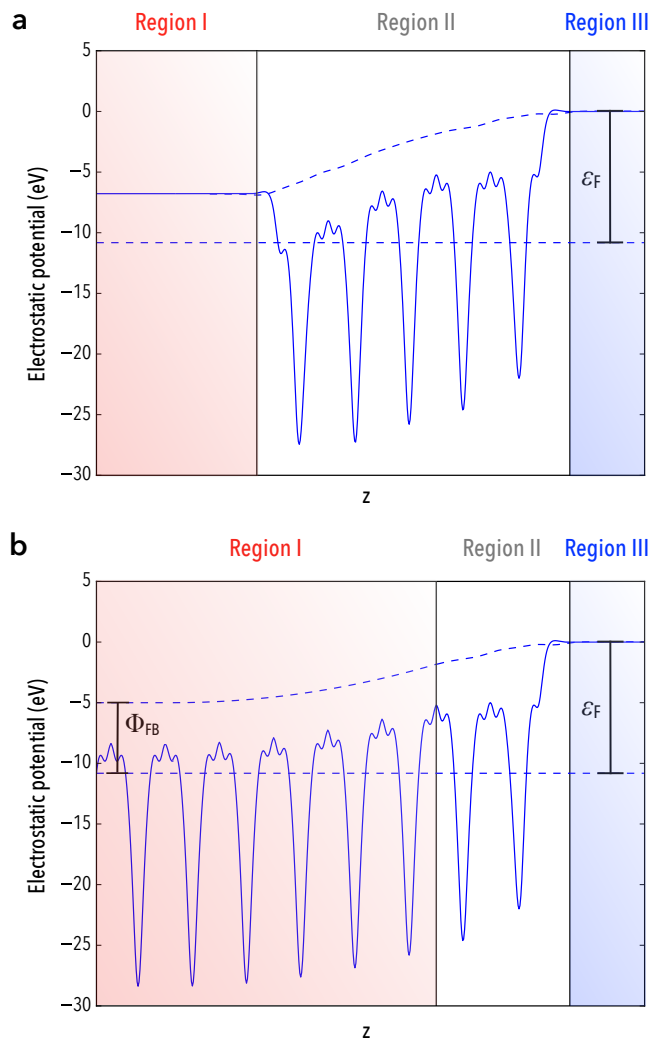


FIG. 3. (a) The potential of a charged slab with planes of countercharge on each side, creating a potential drop. The dotted line represents the electrostatic potential $\bar{\varphi}$ of the charged slab subtracted from that of a slab with zero charge as shown in Fig. 2. (b) A cutoff value z_c corresponding to the inflection of the potential $\bar{\varphi}$ is determined. To the left of this cutoff a Mott–Schottky extrapolation is applied, as shown by the new dotted line. A dichotomy procedure on the surface charge is then applied to match the Fermi levels of Region (I) and Region (II). The width of the depletion region is shortened here for illustrative purposes and would normally extend for several nanometers.

a reliable representation of the electrostatics of a semiconductor electrode where Region (I) consists of an infinite extension of Region (II). To accurately describe the electrostatic potential in Region (I), a cutoff plane is introduced within the slab as illustrated in Fig. 3, and the electrostatic potential to the left of the cutoff is set to follow the solution of the electrostatic equations of a continuum dielectric. The region to the right of the cutoff (but still within the explicit slab) will be taken as Region (II), representing the surface states. From the value of

the electrostatic potential and its derivative at the cutoff plane, the Fermi level of the bulk of the semiconductor in Region (I) can be easily determined from the Mott–Schottky asymptotics [Eqs. (18) and (19)]:

$$\epsilon_{F,(I)} = \bar{\varphi}_\infty - \Phi_{FB} \quad (20)$$

with

$$\bar{\varphi}_\infty = \bar{\varphi}(z_c) - k_B T - \frac{\epsilon_0 \epsilon_{(I)}}{2N_d} \left(\frac{d\bar{\varphi}}{dz}(z_c) \right)^2 \quad (21)$$

$$\bar{\varphi}_\infty = \bar{\varphi}(z_c) + k_B T + \frac{\epsilon_0 \epsilon_{(I)}}{2P_d} \left(\frac{d\bar{\varphi}}{dz}(z_c) \right)^2 \quad (22)$$

for n -type and p -type semiconductor, respectively. In these equations, the cutoff position z_c represents the location of the frontier between Region (I) and Region (II) in Fig. 3b and $\bar{\varphi}$ is the difference between the electrostatic potential of the charged slab [Fig. 3a] and that of the neutral slab [Fig. 2], corresponding to the dashed line in Fig. 3a.

Finally, to find the equilibrium state of the charge electrode, we impose that the Fermi level of the bulk of the semiconductor must equal the Fermi level of the quantum slab:

$$\epsilon_{F,(I)} = \epsilon_{F,(II)}. \quad (23)$$

By fulfilling this condition, one can calculate the dependence of the charge density as a function of voltage, and the surface state density can finally be obtained as the total charge on the right hand side of the frontier defined by z_c divided by the elementary charge e_0 . This computational protocol provides a straightforward and robust method to determine how surface states and adsorption affect the potential distribution and capacitance of the system. This approach is, however, limited in two respects.

First, the position of the frontier between Region (I) and Region (II) defined by z_c may affect the asymptotic value $\bar{\varphi}_\infty$ of the potential $\bar{\varphi}$ describing the overall trend of the potential φ across the interface. This variation is, however, small and can be easily evaluated from $\Delta\bar{\varphi}_\infty = \Delta z_c \frac{d\bar{\varphi}}{dz}(z_c) / \mathcal{L}_{(I)}$, where $\mathcal{L}_{(I)}$ is the electrostatic screening length of the semiconductor; however, since the screening length $\mathcal{L}_{(I)}$ is on the order of 10 – 10^3 nm, the sensitivity of $\bar{\varphi}_\infty$ to z_c is negligible under relevant doping conditions.

Second, the range of charge that can be tested is dependent on the size of the slab. In fact, if the voltage drop between the two countercharge planes is larger than the band gap of the material, unphysical charge transfer by Zener tunneling will take place between the two sides of the slab. In these cases, smaller slabs serve to reduce the voltage drop for a constant Helmholtz charge density. It is important, however, to verify that the Fermi level converges with respect to the size of the slab used for the calculation. Alternatively, this problem can be solved by

implementing a fully self-consistent solution to Eq. (12) in order to eliminate the unphysical slope of the electrostatic potential across the slab due to the absence of screening by the charged defects in Fig. 3a. We plan to implement this alternative method in the continuation of the present work, and we use, for the moment, the implementation described above to assess the predictive performance of the model.

III. COMPUTATIONAL DETAILS

Density-functional theory calculations are performed using the PW code of the Quantum-Espresso distribution.³⁰ Surface slabs of Si(110), SiO₂(110), and rutile TiO₂ are created with a width of 5 layers, which is sufficient to give converged Fermi levels within 0.01 eV. The slab is centered in the supercell with a vacuum height of 7 Å to ensure convergence of the atomic forces within 10^{-3} a.u. We use ultrasoft pseudopotentials with the Perdew–Burke–Ernzerhof parameterization of exchange–correlation interactions.³¹ The cutoffs of kinetic energy of the charge density and electrons are set at 50 Ry and 750 Ry, respectively. The Brillouin zone is sampled with a shifted $5 \times 5 \times 1$ Monkhorst–Pack grid and 0.03 Ry of Marzari–Vanderbilt smearing. The DFT+ U approximation³² is used to correct for electronic self-interaction with a Hubbard parameter value of 2.5 eV for Ti based on the work of Hu and Metiu.³³ As explained above, the electrostatic response of the electrolyte interface is modeled using the ENVIRON module with the parameterizations developed for water by Andreussi et al.²⁴ Several different surface configurations of the TiO₂ surface are examined. In finding the equilibrium structure for these configurations, the middle layer of the slab is frozen and the structure is relaxed. The equilibrium positions are then used in the semiconductor–interface model discussed above. To find the equilibrium charge distribution between the surface states and the bulk of the semiconductor, several different distributions of charge between $q_{(I)}$ and $q_{(II)}$ are tested for a fixed $q_{(III)}$. In specific terms, a dichotomy procedure is employed to match the Fermi levels between the bulk and the surface. We use the cutoff value and charge distribution that minimizes the difference in Fermi level between Regions (I) and (II) with a cutoff position z_c in the middle layers of the slab where the material enters a bulk-like state.

IV. RESULTS AND DISCUSSION

Silicon electrodes represent an important test for the proposed method. When charge is placed on a slab of silicon with planes of countercharge, all of the electronic charge accumulates at the semiconductor edge.³⁴ This contrasts strongly with the expected electron distribution throughout the material, implying that all the charge on

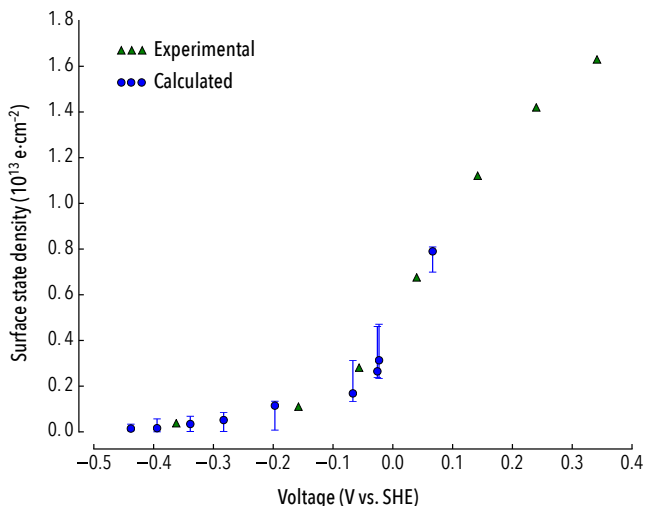


FIG. 4. The surface state density as a function of the electrode potential for SiO_2 , compared with the experimental data of Chandrasekaran et al.³⁸ The dots represent the positions of minimum difference between the Fermi level in Region (I) and Region (II). The error bars show the range of results seen with a tolerance in the Fermi level matching of 0.01 eV.

a silicon semiconductor slab would tend to accumulate deep inside the bulk of the semiconductor, indicating that no surface states would exist. As a result, there is no combination of charges $q_{(I)}$ and $q_{(II)}$ that equalizes the Fermi levels in Region (I) and Region (II) [Eq. (23)]. This suggests that no equilibrium charge distribution exists between the surface of silicon and its bulk state, offering conclusive insights into the instability of pure silicon in water at low potentials.³⁵

Simulations with both hydrogen and oxygen attached to the surface of the silicon slab show charge distributed throughout the material but still do not result in an equilibrium charge distribution between the bulk and the surface. In contrast, simulations using SiO_2 as the surface layer show a distributed charge profile, enabling the Fermi levels in Region (I) and Region (II) to equilibrate, in accordance with suggestions from experimental studies.^{36,37}

To assess the validity of this prediction, we compare our results to accurate experimental measurements that take into account surface states in the analysis of silicon electrodes. The dependence of the surface state density as a function of the potential produced by Chandrasekaran et al.³⁸ for Si(110) is shown in Fig. 4, also including our SiO_2 results. The agreement between these results strongly suggests that in the preparation of their sample, a SiO_2 -like layer forms at the surface of the Si sample, causing the response shown. This is entirely possible, since the authors washed the electrode in water before eventual contact with the electrolyte and the structure was not reexamined after this step.

In Fig. 4, it should be noted that the calculated points

represent the values of the surface charge at which the calculated Fermi levels match the most closely. The error bars show the range of results seen when the tolerance for matching Fermi levels is set to 0.01 eV. This range is not always the same and the error bar increases in regions where the slope of the charge–voltage graph changes rapidly. Due to the fact that the potential across the semiconductor slab cannot be greater than the band gap or the electrode, the calculated points necessarily stops at some voltage. These results differ from what would be expected if solely the bulk of the semiconductor was taken into account in a standard Mott–Schottky treatment. The measurements of Chandrasekaran et al.^{38–40} have consistently shown that at higher potentials, the charge–voltage response follows the square root dependence that would be expected from the Mott–Schottky theory. The onset of the square root behavior is seen in the experimental high-voltage region of Fig. 4, while the proposed method provides a detailed understanding of the low-potential regime where charges on the surface states dominate the overall behavior of the electrode system, which is not captured by a purely classical Mott–Schottky approach.

Additionally, the dependence of the charge density of TiO_2 electrodes on the potential is reported in Fig. 5. Here, the referenced value of the flatband potential is aligned to the experimental measurement of Nakamura et al.⁴¹ The results match an exponential trend at low potentials, following the behavior discussed above for silicon with a SiO_2 surface layer. The fraction of the total potential taken by each region is dominated by the surface states at potentials close to the flatband potential.³⁴ This can also be seen in the charge versus potential graph where the surface state charge accounts for most of the total charge. The general trend is not strongly affected by the surface structure used, confirming again the central relevance of surface states in the behavior of all TiO_2 electrode surfaces.

While the overall trend is the same for all the observed surface structures, it is instructive to note some important variations. In particular, the structure with an oxygen vacancy shows a noticeably smaller exponential factor. Additionally the surface state charge density falls much lower than the total charge density than is seen in other surface structures. This shows that surface states are less dominant in an oxygen vacancy structure than in other common TiO_2 surface configurations. This results is of practical interest in explaining the behavior of reduced TiO_2 surfaces, where oxygen vacancy structures dominate the charge–voltage response.⁴²

V. CONCLUSION

Semiconductor–electrolyte interfaces encompass a multitude of applications at the frontier of solid state physics and photoelectrochemistry. We have presented a method to integrate first-principles calculations of surface state

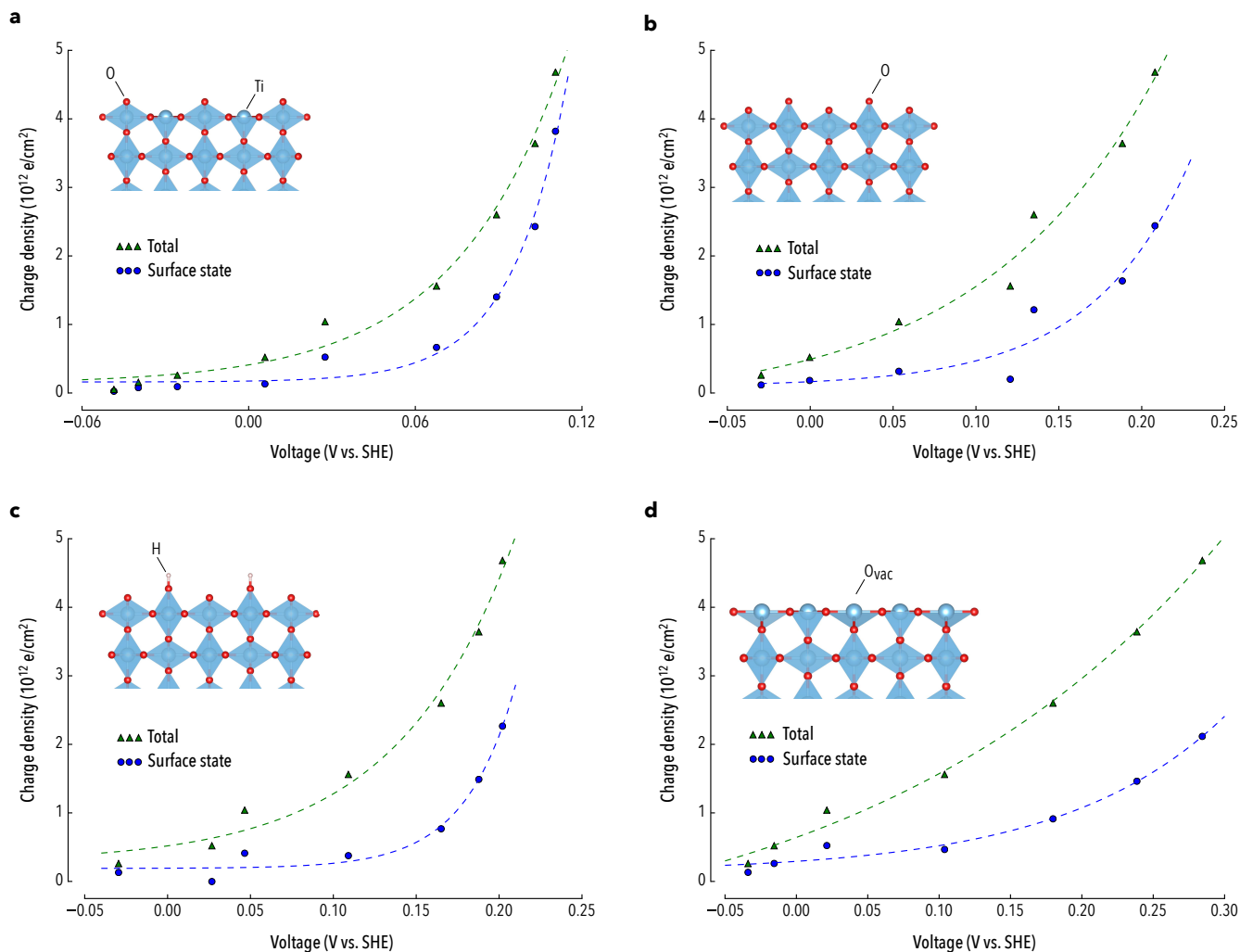


FIG. 5. The charge density versus potential plots for several different surface configurations of rutile $\text{TiO}_2(110)$. The surfaces represented are (a) stoichiometric, (b) oxygenated, (c) hydroxylated, (d) and with an oxygen vacancy. The dotted lines correspond to exponential fits of the data.

energies with the Mott–Schottky model of band bending in semiconductors. We have validated our method on several different surfaces of rutile $\text{TiO}_2(110)$ and $\text{Si/SiO}_2(110)$. Our simulations show conclusive agreement with experiment and provide a molecular-level understanding of the experimentally observed instability of silicon electrodes in water, suggesting a possible equilibrium structure for silicon–water interface consisting of a surface layer of SiO_2 for the equilibration of the bulk and interfacial Fermi levels. This method is well positioned to examine the low-potential regime where surface state charges dominate the electrical response of the electrode in a manner not captured by the continuum Mott–Schottky theory alone.

Future work will focus on extending the method to implement and distribute robust algorithms that self-

consistently determine the equilibrium distribution of charge between the bulk of the semiconductor and the surface states using a variational method relying on the free energy expression developed in this work. These computational implementations will allow systematic studies of a diversity of semiconductor–electrolyte interfaces in an effort to understand, predict, and optimize their equilibrium structure and electrical response under realistic ionic activities and interfacial electrification.

ACKNOWLEDGMENTS

The authors acknowledge financial support from the 3M Fellowship and Penn State University Graduate Fellowship.

* qjc5019@psu.edu

¹ A. Kudo and Y. Miseki, *Chemical Society Reviews* **38**, 253

- (2009).
- ² S. C. Roy, O. K. Varghese, M. Paulose, and C. a. Grimes, *ACS Nano* **4**, 1259 (2010).
 - ³ R. Tenne and G. Hodes, *Surface Science* **35**, 453 (1983).
 - ⁴ X. Jin, P. Gao, D. Wang, X. Hu, and G. Z. Chen, *Angewandte Chemie* **43**, 733 (2004).
 - ⁵ K. Peng, H. Fang, J. Hu, Y. Wu, J. Zhu, Y. Yan, and S. Lee, *Chemistry - A European Journal* **12**, 7942 (2006).
 - ⁶ X. Xia, J. Tu, Y. Zhang, X. Wang, C. Gu, X. Zhao, and H. J. Fan, *ACS Nano*, 5531 (2012).
 - ⁷ R. Gill, M. Zayats, and I. Willner, *Angewandte Chemie* **47**, 7602 (2008).
 - ⁸ M. D. Bhatt and J. S. Lee, *Journal of Materials Chemistry A* **3**, 10632 (2015).
 - ⁹ I. E. Castelli, D. D. Landis, K. S. Thygesen, S. Dahl, I. Chorkendorff, T. F. Jaramillo, and K. W. Jacobsen, *Energy & Environmental Science* **5**, 9034 (2012).
 - ¹⁰ I. E. Castelli, F. Huser, M. Pandey, H. Li, K. S. Thygesen, B. Seger, A. Jain, K. A. Persson, G. Ceder, and K. W. Jacobsen, *Advanced Energy Materials* **5**, 1 (2015).
 - ¹¹ Y. Ping, R. Sundararaman, and W. A. Goddard Iii, *Physical chemistry chemical physics* **17**, 30499 (2015).
 - ¹² Y. Ping, W. A. Goddard, and G. A. Galli, *Journal of the American Chemical Society* **137**, 5264 (2015).
 - ¹³ H. Cheng and A. Selloni, *Langmuir* **26**, 11518 (2010).
 - ¹⁴ Y. Wu, M. K. Y. Chan, and G. Ceder, *Physical Review B* **83**, 1 (2011).
 - ¹⁵ S. Yang, D. Prendergast, and J. B. Neaton, *Nano Letters* **12**, 383 (2012).
 - ¹⁶ M. Setvin, U. Aschauer, J. Hulva, T. Simschitz, B. Daniel, M. Schmid, A. Selloni, and U. Diebold, *Journal of the American Chemical Society* **138**, 9565 (2016).
 - ¹⁷ Y. F. Li and A. Selloni, *ACS Catalysis* **6**, 4769 (2016).
 - ¹⁸ T. Cheng, H. Xiao, and W. A. Goddard, *Journal of the American Chemical Society*, jacs.6b08534 (2016).
 - ¹⁹ M. Oshikiri and M. Boero, *The Journal of Physical Chemistry B* **110**, 9188 (2006).
 - ²⁰ J. B. Rivest, G. Li, I. D. Sharp, J. B. Neaton, and D. J. Milliron, *Journal of Physical Chemistry Letters* **5**, 2450 (2014).
 - ²¹ J. H. Lee and A. Selloni, *Physical Review Letters* **112**, 1 (2014).
 - ²² G. A. Tritsarlis, D. Vinichenko, G. Kolesov, C. M. Friend, and E. Kaxiras, *The Journal of Physical Chemistry C* **118**, 27393 (2014).
 - ²³ K. Rajeshwar, in *Encyclopedia of Electrochemistry* (2007).
 - ²⁴ O. Andreussi, I. Dabo, and N. Marzari, *Journal of Chemical Physics* **136** (2012).
 - ²⁵ N. Bonnet and N. Marzari, *Physical Review Letters* **110**, 1 (2013).
 - ²⁶ L. Sementa, O. Andreussi, W. A. Goddard III, and A. Fortunelli, *Catal. Sci. Technol.* **6**, 6901 (2016).
 - ²⁷ M. M. Montemore, O. Andreussi, and J. W. Medlin, *Journal of Chemical Physics* **145** (2016), 10.1063/1.4961027.
 - ²⁸ N. Keilbart, Y. Okada, S. Higai, and I. Dabo, Submitted (2016).
 - ²⁹ S. Weitzner and I. Dabo, Submitted (2016).
 - ³⁰ P. Giannozzi, S. Baroni, N. Bonini, M. Calandra, R. Car, C. Cavazzoni, D. Ceresoli, G. L. Chiarotti, M. Cococcioni, I. Dabo, A. Dal Corso, S. de Gironcoli, S. Fabris, G. Fratesi, R. Gebauer, U. Gerstmann, C. Gougousis, A. Kokalj, M. Lazzeri, L. Martin-Samos, N. Marzari, F. Mauri, R. Mazzarello, S. Paolini, A. Pasquarello, L. Paulatto, C. Sbraccia, S. Scandolo, G. Sclauzero, A. P. Seitsonen, A. Smogunov, P. Umari, and R. M. Wentzcovitch, *Journal of Physics: Condensed Matter* **21**, 395502 (2009).
 - ³¹ J. P. Perdew, K. Burke, and M. Ernzerhof, *Physical Review Letters* **77**, 3865 (1996).
 - ³² M. Cococcioni and S. de Gironcoli, *Physical Review B* **71**, 035105 (2005), arXiv:0405160 [cond-mat].
 - ³³ Z. Hu and H. Metiu, *Journal of Physical Chemistry C* **115**, 5841 (2011).
 - ³⁴ See Supplementary Material at xx for the graphical depiction of the cumulative charge distribution of Si, SiO₂, TiO₂, and the contributions from the surface states to the screening of the electrostatic potential at the interface.
 - ³⁵ P. A. Nikolaychuk, *Silicon* **6**, 109 (2014).
 - ³⁶ W. R. Runyan, in *Kirk-Othmer Encyclopedia of Chemical Technology* (2013) pp. 1–22.
 - ³⁷ D. Graf, M. Grundner, and R. Schulz, *Journal of Vacuum Science & Technology A* **7**, 808 (1989).
 - ³⁸ K. Chandrasekaran, R. C. Kainthla, and J. O. Bockris, *Electrochimica Acta* **33**, 327 (1988).
 - ³⁹ K. Chandrasekaran and J. O. M. Bockris, *Electrochimica Acta* **32**, 1393 (1987).
 - ⁴⁰ K. Chandrasekaran, M. Weichold, F. Gutmann, and J. O. M. Bockris, *Electrochimica Acta* **30**, 961 (1985).
 - ⁴¹ R. Nakamura, T. Okamura, N. Ohashi, and A. Imanishi, *Journal of the American Chemical Society* **2**, 431 (2005).
 - ⁴² P. M. Kowalski, B. Meyer, and D. Marx, *Physical Review B* **79**, 115410 (2009).